A&A, 706, A30 (2026)
https://doi.org/10.1051/0004-6361/202556898

Astronomy & Astrophysics

Heavy-element-enriched atmospheres and where they are born

Barry O'Donovan[1,2,⋆] and Bertram Bitsch[1,⋆]

[1] Department of Physics, University College Cork, Cork, Ireland
[2] School of Physics, Trinity College Dublin, University of Dublin, Dublin 2, Ireland

Received 18 August 2025 / Accepted 3 December 2025

ABSTRACT

The heavy element content of giant exoplanets, inferred from structure models based on their radius and mass, often exceeds predictions based on classical core accretion. Pebble drift, coupled with volatile evaporation, has been proposed as a possible remedy to this since the level of heavy element enrichment a planet can accrete, as well as its atmospheric composition, is strongly dependent on where in the disc it is forming. We used a planet formation model that simulates the evolution of the protoplanetary disc, accounting for pebble growth, drift and evaporation, and the formation of planets from pebble and gas accretion. We simulated the growth and migration of planetary embryos in ten different protoplanetary discs whose chemical compositions are matched to the host stars of the planets that we aim to reproduce; this provided a more realistic model of their growth than previous studies. The heavy element content of giant exoplanets was used to infer their formation location and thus to estimate their atmospheric abundances. We focused on giants more massive than Saturn, as we expect that their heavy element content is dominated by their envelope rather than their core. The heavy element content of nine out of the ten simulated planets is successfully matched to their observed values. Our simulations predict formation in the inner disc regions, where the majority of the volatiles have already evaporated and can thus be accreted onto the planet via the gas. As the majority of the planetary heavy element content originates from water vapour accretion, our simulations predict a high atmospheric O/H ratio in combination with a low atmospheric C/O ratio, which is in general agreement with observations. For certain planets, namely WASP-84b, these properties may be observable in the near future, offering a method of testing the constraints placed on the planet's formation.

Key words. planets and satellites: atmospheres – planets and satellites: composition – planets and satellites: formation – planets and satellites: gaseous planets – protoplanetary disks

1. Introduction

The past two decades have seen an explosion in exoplanet discoveries, revealing an extraordinary diversity of planetary systems unlike our own (Winn & Fabrycky 2015). Among these, gas giants remain critical to our understanding of planet formation. Their prevalence, wide range of densities, and large radii make them both accessible to observation and influential in shaping planetary system architectures. Their formation not only affects the distribution and availability of materials for other forming planets (e.g. Lambrechts et al. 2014; Bitsch et al. 2018) but also influences orbital dynamics and stability within planetary systems (e.g. Beaugé & Nesvorný 2012; Schlecker et al. 2021; Bitsch & Izidoro 2023), with important consequences for the presence of habitable planets (e.g. Georgakarakos et al. 2018; Agnew et al. 2019).

Classically, gas giant formation is understood via the core accretion paradigm: dust grains coagulate into pebbles and planetesimals and form a solid core (~10 $M_\oplus$), which then accretes gas from the protoplanetary disc once the pebble isolation mass threshold is reached (e.g. Pollack et al. 1996; Mordasini et al. 2012). The pebble-accretion variant enables rapid core growth via the aerodynamic drag of millimetre- to centimetre-sized particles (e.g. Ormel & Klahr 2010; Lambrechts & Johansen 2012). Throughout growth, forming planets migrate via disc–planet torques (Type I) and eventually open gaps (Type II), moving across diverse disc regions that differ in temperature and composition (e.g. Öberg et al. 2011; Madhusudhan et al. 2014; Turrini et al. 2021; Bitsch et al. 2022; Penzlin et al. 2024).

A major challenge to these models arises from the observations of Thorngren et al. (2016), who analysed 47 transiting giant exoplanets and derived their heavy-element masses (M_Z) using interior structure models (later confirmed by Bloot et al. 2023). Thorngren et al. (2016) found that many giant planets host over 50–100 $M_\oplus$ in heavy elements, indicating that many giant exoplanets contain significantly higher masses of heavy elements compared to the giant planets in our own Solar System, such as Jupiter and Saturn (Vazan et al. 2018). These high heavy element contents are also confirmed by more advanced interior models that take different internal structures into account (Peerani et al. 2026). These heavy element measurements are often too large to be confined solely to the core and imply a heavy element enrichment of the gaseous envelope itself. Moreover, this enrichment shows only a weak correlation with host-star [Fe/H], in contrast to earlier expectations (Teske et al. 2019). This poses a puzzle: classical formation pathways struggle to explain giant planets that are so highly enriched with heavy elements, especially when the metallicity of the host star is not extremely high (Venturini & Helled 2020). A solution to this problem could be found in collisions between growing planets whose envelopes are stripped while retaining the heavy element mass of their cores (e.g. Ogihara et al. 2021). However, the remaining systems in these models still contain multiple planets, whereas hot Jupiters, as used in the sample of Thorngren et al. (2016), are mostly single planets (e.g. Dawson & Johnson 2018).

⋆ Corresponding authors: bbitsch@ucc.ie; odonovb3@tcd.ie

Pebble drift and evaporation at volatile evaporation fronts offers a solution to this puzzle by allowing heavy elements to be transported efficiently through the disc and be accreted into the atmospheres of growing planets. As pebbles drift inwards and evaporate at volatile evaporation fronts, they enrich the surrounding gas with heavy elements, which can then be accreted by forming gas giants (e.g. Booth et al. 2017; Schneider & Bitsch 2021). Models that account for this process yield results that are in slightly better agreement with the observations of Thorngren et al. (2016) compared to the classical core accretion scenario (e.g. Schneider & Bitsch 2021; Morbidelli et al. 2023; Bitsch & Mah 2023). But in order to accurately model the formation of a specific planet, one must account for the natal disc chemistry of the planet's birth environment. The initial chemical composition of the protoplanetary disc can be assumed to be the same as that of its host star (e.g. Hühn & Bitsch 2023) as the two formed from the same cloud of gas and dust. So, the detailed stellar abundance measurements of Teske et al. (2019), which include 18 of the host stars of the planets from the Thorngren et al. (2016) dataset, allow us to model the growth and evolution of these planets in discs with chemical compositions matched to their birth environment. This is a major improvement over older models that assume solar-scaled abundances (e.g. Schneider & Bitsch 2021; Bitsch & Mah 2023) and can help explain the observations of Thorngren et al. (2016).

Atmospheric characterisation has entered a golden era thanks to instruments like JWST (Bean et al. 2023; Taylor et al. 2023). Transmission spectroscopy is now capable of detecting molecules such as H_2O, CO_2, CH_4, and sulphur compounds in the atmospheres of transiting giants (e.g. WASP-39b; Lueber et al. 2024; Powell et al. 2024) and retrieving their C/O ratios and metallicities (e.g. Kreidberg et al. 2014; August et al. 2023; Evans-Soma et al. 2025). These atmospheric abundances hold vital clues about the conditions under which planets formed, including their initial positions within the disc, their migration pathways, and the timing and nature of material accretion, offering a new route to validate or refute planet formation scenarios (Madhusudhan et al. 2017; Booth & Ilee 2017; Schneider & Bitsch 2021; Mollière et al. 2022; Bitsch et al. 2022; Penzlin et al. 2024; Ohno et al. 2025).

We used the `Chemcomp` code (Schneider & Bitsch 2021) to model the growth and migration of the planets in the Thorngren et al. (2016) sample for which stellar abundances are available (Teske et al. 2019). We reproduced the heavy element content of the giant planets within this sample, which we then used to derive their formation location.

2. Methodology

2.1. General methods

The `Chemcomp` planet formation code (Schneider & Bitsch 2021) is a numerical model designed to simulate the formation of giant planets within protoplanetary discs. Its operation principle involves simulating key processes such as gas and pebble evolution within the disc, planet formation, and planetary migration.

Initially, the model defines a protoplanetary disc with specific initial parameters such as mass (M_0), radius (R_0), initial metallicity (ϵ_0), and chemical composition. The disc structure, described by the gas surface density $\Sigma_{\rm gas}$ and temperature T, is a power-law profile determined by stellar heating and viscous accretion (e.g. Lynden-Bell & Pringle 1974; Bell et al. 1997), governed by the viscosity parameter (α) from Shakura & Sunyaev (1973):

$$\nu = \alpha \frac{c_s^2}{\Omega_K}, \tag{1}$$

where c_s is the sound speed and Ω_K is the Keplerian angular velocity.

The isothermal sound speed, c_s, is related to the disc midplane temperature, $T_{\rm mid}$, through

$$c_s = \sqrt{\frac{k_B T_{\rm mid}}{\mu m_p}}, \tag{2}$$

where μ is the mean molecular weight and m_p the proton mass. Variations in μ can occur if the gas is enriched with vapour.

We used a stellar luminosity of $1 L_\odot$ throughout as this roughly corresponds to the stellar luminosity of stars of age 1.5–2.0 Myr (Baraffe et al. 2015). Viscous heating dominates the temperature profile in the inner disc while stellar irradiation only plays a large role in the outer regions (Bitsch et al. 2013). We focused in our study on the inner disc regions, where the heavy element enrichment in the gas phase is largest (e.g. Bitsch & Mah 2023), indicating that a change in the stellar luminosity would not influence our results.

The viscosity (ν) directly influences how quickly material moves radially inwards through the disc and onto the star, a process known as viscous accretion. This radial transport is described mathematically by the viscous disc equation (Pringle 1981; Armitage 2013) for the gas surface density ($\Sigma_{\rm gas}$):

$$\frac{\partial \Sigma_{\rm gas,\,y}}{\partial t} - \frac{3}{r}\frac{\partial}{\partial r}\left[r^{1/2} \frac{\partial}{\partial r}\left(\nu \Sigma_{\rm gas,\,y} r^{1/2} \right) \right] = \dot{\Sigma}_Y, \tag{3}$$

where $\dot{\Sigma}_Y$ is a source term for a given chemical species Y, described below.

Dust grains within the disc grow into pebbles via coagulation; we followed the approach of Birnstiel et al. (2012). The inward radial drift speed (u_Z) was determined by their Stokes number (St):

$$\mathrm{St} = \frac{\pi}{2}\frac{a \rho_\bullet}{\Sigma_{\rm gas}}, \tag{4}$$

with pebble radius a and density $\rho_\bullet$. These pebbles drift towards the star and evaporate upon crossing evaporation lines, enriching the gas in heavy elements like water (H_2O) and carbon-bearing species. This enhances the availability of these elements for gas accreting planets forming in these regions, as they accrete the vapour via the gas.

We modelled the evaporation and condensation of material by including a corresponding term in the viscous evolution equation (Eq. (3)). We assumed that the inward drifting pebbles would evaporate within 10^{-3} AU.

Planets in `Chemcomp` first grow by accreting pebbles, calculated using pebble accretion rates ($\dot{M}_{\rm peb}$; Johansen & Lambrechts 2017), until they reach a critical mass called the pebble isolation mass (Lambrechts et al. 2014; Bitsch et al. 2018; Ataiee et al. 2018) at which point the planet's gravity is strong enough to alter the flow of gas and pebbles around it and opens a gap that blocks inward drifting pebbles. Once the planet reaches the pebble isolation mass, defined as

$$M_{\rm iso} \approx 25 \left(\frac{H/r}{0.05} \right)^3 M_\oplus, \tag{5}$$

with H/r being the disc's aspect ratio, pebble accretion ceases, and gas accretion ($\dot{M}_{\rm gas}$) commences.

Planets migrate first in the type-I regime; we followed the prescription of Paardekooper et al. 2011. We additionally included effects from dynamical torques (Paardekooper 2014) as well as from the heating torque (Benítez-Llambay et al. 2015) that act to slow the inward migration in the type-I migration regime and could, in some cases, even promote outward migration. Once the planets start to open gaps, their migration rate slows and they migrate in the slower type-II migration regime with the viscous rate.

2.2. Chemistry

We used `Chemcomp` (Schneider & Bitsch 2021) to simulate the growth and migration of planetary embryos with the goal of matching the heavy element contents of the giant planets measured by Thorngren et al. (2016) In addition, we used the detailed stellar abundances of Teske et al. (2019) as a constraint for our chemical model. This allows the growth of planets to be simulated in discs with chemical compositions matched to their birth environments. We only simulated the growth of the planets heavier than 0.5 M_J for which host star abundances were available from Teske et al. (2019). We focused on these massive planets because their compositions are dominated by gaseous envelopes, making their enrichment more difficult to explain using standard models. In contrast, lower-mass planets ($M \ll M_J$) can often match their observed heavy element mass through large solid cores alone (the pebble isolation mass can easily be 10–20 $M_\oplus$ alone; see Bitsch et al. 2018). Therefore, the most massive planets offer a more stringent test of planet formation theories. The stellar chemical abundances also allow the initial dust-to-gas ratio (DTG) in each disc to be calculated according to the following equation from Andama et al. (2024):

$$\mathrm{DTG} = \sum_{\mathrm{X}} \left(\mathrm{X/H} \cdot \mu_{\mathrm{X}} \times 10^{[\mathrm{X/H}]} \right), \tag{6}$$

where X/H is the abundance (by number) of element X (elements used for DTG calculation are C, O, Mg, Si, S, and Fe) in a solar-like disc (Asplund et al. 2009), μ_{X} is the atomic mass of element X, and [X/H] is the logarithmic abundance of element X relative to hydrogen, measured in units of dex, from Teske et al. (2019). The elements included in our simulations are H, He, C, O, Mg, Si, S, and Fe. Although sulphur is not included in the abundance measurements of Teske et al. (2019), we can assume that it scales in the same way as silicon (Chen et al. 2002). The initial elemental abundances used in the simulations of each disc along with the DTGs and stellar masses are shown in Table A.1.

Measurements based on solar photospheric and meteoritic CI chondrite abundances suggest that only about 10% of carbon is found in refractory form, with the remaining 90% in volatile molecules (Lodders 2003). Cometary data suggest a slightly higher refractory fraction of around 20% (Altwegg et al. 2020), while interstellar medium observations point to much higher values, with up to 60% of carbon in refractory grains (Bergin et al. 2015). In this paper, simulations are run with a refractory carbon fraction of 60%, consistent with interstellar medium values. This is also consistent with previous studies on giant planet formation and disc chemistry (e.g. Schneider & Bitsch 2021; Mah et al. 2023). We did not include the option of refractory carbon burning (e.g. Houge et al. 2025) in our model, as this effect does not influence the source of the heavy element content of the planets in our model: the majority of the heavy elements are accreted with the gas exterior to the carbon burning front during planet growth. Furthermore, it does not influence the overall message and idea of our work: constraining the origin of the planet via their total heavy element contents.

2.3. Model parameters

Simulations are run for viscosity values of $\alpha = 1 \times 10^{-4}$, $\alpha = 5 \times 10^{-4}$ and $\alpha = 1 \times 10^{-3}$. Figure 1 shows how a planet's growth and composition varies with different disc viscosities. The timing of a planet's heavy element accretion is heavily dependent on the viscosity of the disc. The early stage of planet growth is the pebble accretion phase where growth is determined by the pebble flux and pebble sizes. In the lower-viscosity settings ($\alpha = 1 \times 10^{-4}$, $\alpha = 5 \times 10^{-4}$) these are both larger than for high viscosities, and so the core grows slightly faster in these settings. However, once the pebble isolation mass is reached, the accretion rate is limited by the gas accretion rate, which is set by the viscous accretion rate of the disc. There a higher viscosity ($\alpha = 1 \times 10^{-3}$) automatically results in a faster accretion rate ($\dot{M}_{\rm disc} \propto \nu$). As the majority of the giant planet is composed of gas, this sets the growth time of the planet. All simulations are run with a disc mass of 0.128 $M_\odot$ and a disc radius of 137AU (Schneider & Bitsch 2021), a large disc mass is chosen to grow the giant planets efficiently following the idea of Savvidou & Bitsch (2023). The grain fragmentation velocity used in the simulations is 5 m s^{-1} and planetary embryos are initially placed at 0.1 Myr with an initial embryo mass of 0.005 $M_\oplus$.

To compare with observations, the output from each simulation is evaluated at the timestep when the simulated planet reaches the observed mass of its corresponding planet from the dataset. While we adopted a fiducial disc lifetime of 3 Myr (this is extended for low viscosities), this method accounts for the fact that protoplanetary discs may disperse earlier in reality (Mamajek 2009). For low viscosities ($\alpha = 1 \times 10^{-4}$), long disc lifetimes were required to allow the formation of the most massive planets for planetary embryos originating interior to the water-ice line due to the slow transport of solid material to the inner disc. Kepler-419b, for example, which has a mass of $\sim 2.5 M_J$ would have taken $\sim$17 Myr to grow to its observed mass if it originated at 0.3AU in a disc of $\alpha = 1 \times 10^{-4}$. HD 80606b (3.94 M_J) and Kepler-432b (5.84M_J) would have taken $\sim$12 Myr for the same initial scenario. It should be noted that for this initial scenario the planets form with low heavy element masses. For Kepler-419b and HD 80606b the final simulated heavy element masses for an initial embryo position of 0.3AU are below the uncertainty range from Thorngren et al. (2016) and so this formation scenario can be dismissed. The observed heavy element mass of Kepler-432b is not well constrained (the uncertainty range extends down to 0.1 $M_\oplus$ and so it is very difficult to make a prediction on the planet's formation location in the first place) so while the final simulated heavy element mass for this scenario falls within the uncertainty range we can still dismiss this formation scenario due to the unrealistically long disc lifetime needed to explain its formation. Observations show a spread in disc dispersal timescales, which can be attributed to a range of factors including stellar mass, environment, and photoevaporation rates (Güdel et al. 2007; Owen et al. 2011; Haworth et al. 2018; Picogna et al. 2021; Pfalzner et al. 2022; Haworth et al. 2023). In particular, variation in high-energy radiation (e.g. X-rays) from young stars can drive differing photoevaporation rates, leading to significant diversity in the lifetimes of protoplanetary discs. Once the planet has reached its desired mass, we assume that the disc dissipates. This is modelled by an exponential decay of the

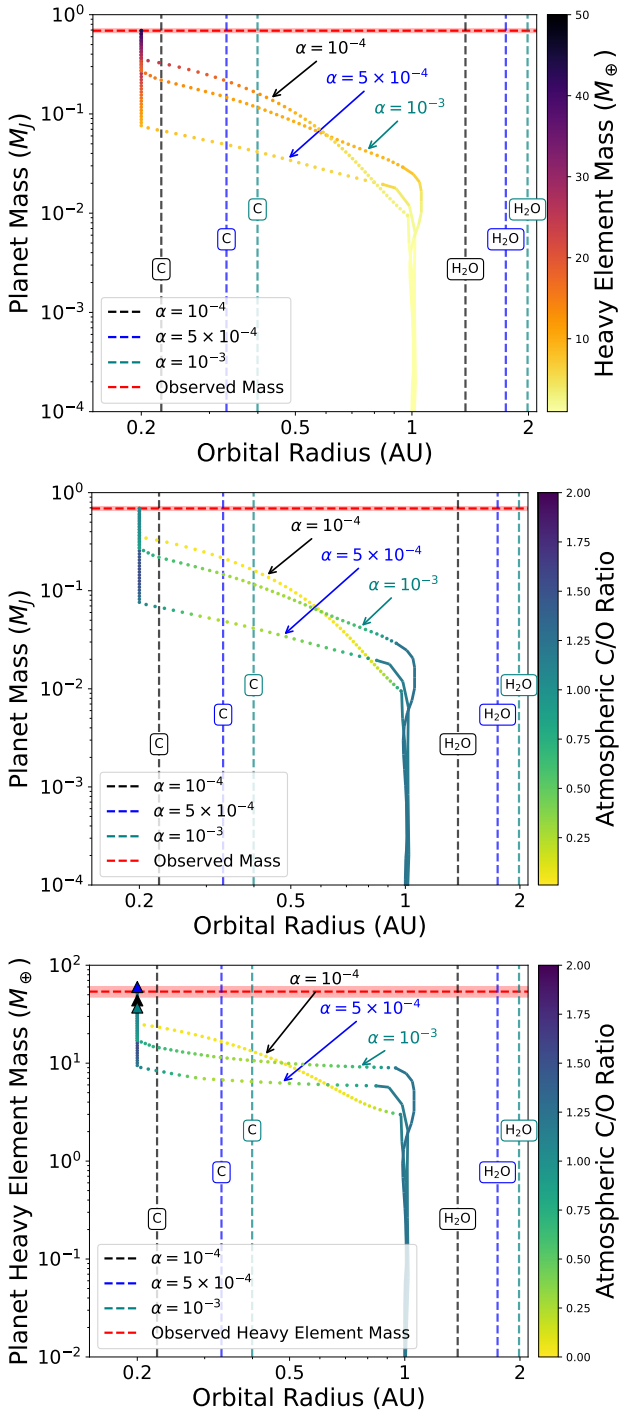

Fig. 1. Growth tracks showing the orbital evolution of a planet simulated in the disc of WASP-84 for three different disc viscosities: $\alpha = 10^{-4}$, $\alpha = 5 \times 10^{-4}$, and $\alpha = 10^{-3}$. The planet originates at an orbital radius of 1 AU and migrates inwards. *Top*: mass evolution of the planet, colour-coded by the planet's heavy element mass. *Middle*: mass evolution of the planet, colour-coded by the planet's atmospheric carbon-to-oxygen ratio. *Bottom*: heavy element mass evolution of the planet colour-coded by the planet's atmospheric carbon-to-oxygen ratio. The locations of the C and H_2O evaporation fronts are shown for the three different viscosities. The horizontal dashed red line and shaded region show the observed mass (top and middle) and the observed heavy element mass (bottom) and their uncertainties. The coloured triangles in the bottom plot show the final simulated heavy element mass for each viscosity. Growth tracks plotted as solid lines indicate that the planet is undergoing pebble accretion, and dotted lines indicate gas accretion.

disc's surface density within a short period of time. While we did not model the exact photo-evaporative profile of the disc, we note that the planetary composition is unaltered within the two approaches (Sheehan et al., in prep.).

We did not compare the final semi-major axes of the simulations as scattering events after the dispersal of the disc could have moved the planet into its observed orbit (Chatterjee et al. 2008; Beaugé & Nesvorný 2012; Paardekooper & Johansen 2018; Bitsch et al. 2020). As scattering events require multiple growing objects it is important to note that the innermost planets grow fastest and are thus only minimally influenced in respect to their composition if outer planets grow afterwards (Eberlein et al. 2024).

In the following section, we discuss how varying the initial position of planetary embryos in the disc allows us to directly match the simulated heavy element masses to observations and the predictions that these simulations make about the composition of each planet's atmosphere.

3. Formation of heavy-element-enriched planets

3.1. Results

In this study, we successfully reproduced the observed heavy element masses for 9 out of the 10 most massive planets from Thorngren et al. (2016), for which stellar abundances observations were available (Teske et al. 2019), for viscosities of $\alpha = 1 \times 10^{-4}$ and $\alpha = 5 \times 10^{-4}$ and 8 out of 10 for $\alpha = 1 \times 10^{-3}$. The simulations could not reproduce the heavy element content of Kepler-539b for any of the viscosity values tested. Kepler-539b is a planet with mass $M = 0.97\,M_J$ and heavy element mass $M_Z = 155\,M_\oplus$, corresponding to an unusually high heavy element fraction of 49%. This level of enrichment makes Kepler-539b much denser than the other planets considered, suggesting that additional processes, such as atmospheric stripping or giant impacts, removed a substantial portion of its hydrogen and helium envelope without significantly reducing its core mass (Louden et al. 2017; Denman et al. 2020). These mechanisms are not currently accounted for in `Chemcomp`.

We matched the heavy element content of the giant planets by simulating the growth of planets with different initial positions of the planetary embryo in order to test which initial position would lead to the planet accreting the observed amount of heavy elements once it reached its observed mass. These results are presented in Fig. 2. For the remainder of the main body of this work we focus on the results from the $\alpha = 1 \times 10^{-4}$ simulations due to the unrealistically rapid planet formation and disc dispersal required to match the heavy element observations for the $\alpha = 5 \times 10^{-4}$ and $\alpha = 1 \times 10^{-3}$ cases. The disc lifetime for a given system was inferred from the timestep at which the simulated planet reached the observed mass and heavy element mass. For the $\alpha = 1 \times 10^{-4}$ discs the inferred lifetimes ranged from 1–10 Myr with the majority of planets forming within 4 Myr, this is in agreement with the observed distribution of protoplanetary disc lifetimes (Mamajek 2009; Pfalzner et al. 2022). For $\alpha = 5 \times 10^{-4}$ discs the inferred lifetimes ranged from 0.2–3 Myr with the majority of planets forming within 1 Myr and for $\alpha = 1 \times 10^{-3}$ all discs were inferred to disperse within 1 Myr. The lifetimes for viscosities larger than $\alpha = 1 \times 10^{-4}$ are not in line with observations. See Appendix B for further justification and an overview of the results for the higher viscosity simulations. Table B.1 explicitly shows the inferred lifetimes of the discs of five of the simulated planets that had well-constrained heavy element masses for the $\alpha = 1 \times 10^{-4}$ case. To illustrate

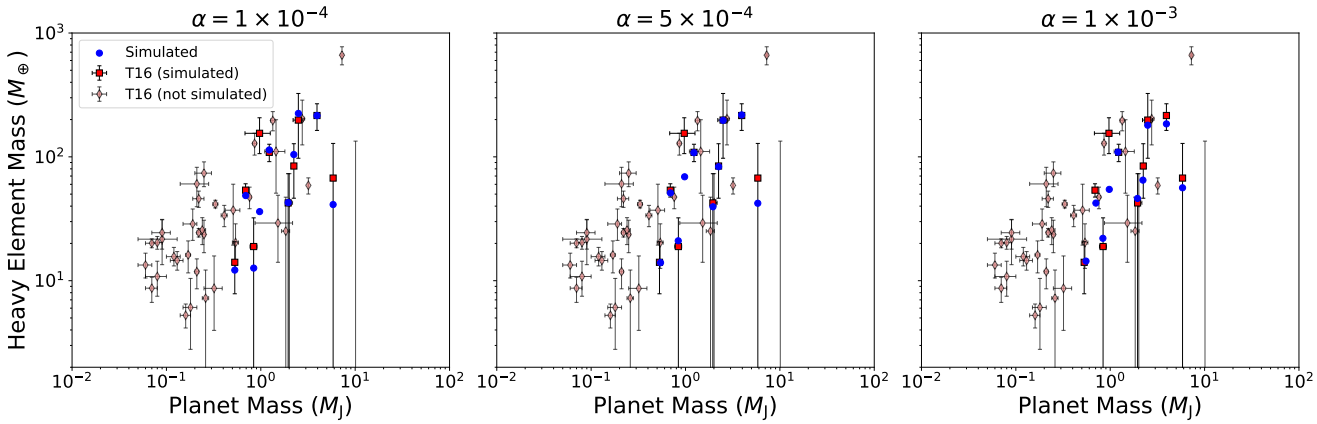

Fig. 2. Mass vs heavy element mass relation for the ten simulated planets. Blue points show simulations where the initial formation location matched the observed heavy element mass most closely. Data from Thorngren et al. (2016) are shown in red (T16). Planets that are simulated in this work are plotted as red squares, while those that are not simulated in this work, either because they are less massive than 0.5 M_J or because the stellar chemical abundances of their host star are not included in Teske et al. (2019), are plotted as pale red diamonds.

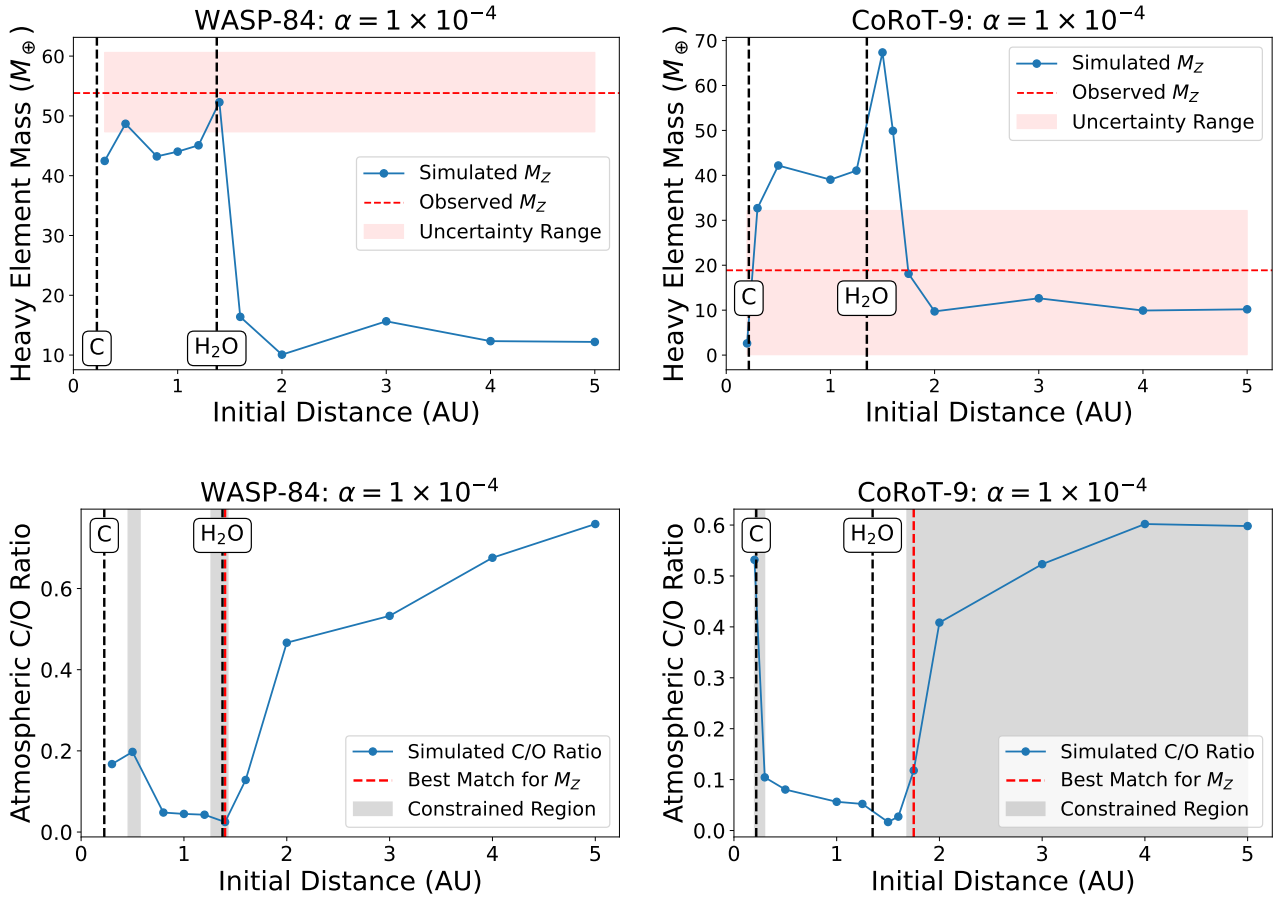

Fig. 3. *Top row*: heavy element masses of the planets simulated in the discs of WASP-84 (*left*) and CoRoT-9 (*right*) as a function of the initial position of the planetary embryo. The observed heavy element mass is shown as a dashed red line, with its uncertainty indicated by a red shaded region. *Bottom row*: predicted atmospheric C/O number ratios of the same planets as a function of initial position. The dashed red line shows the best-fit formation location based on the heavy element mass, and the grey region indicates the constrained range of possible formation locations. H_2O and C evaporation fronts are shown as dashed black lines in all panels. All simulations use $\alpha = 1 \times 10^{-4}$.

the general trend of how the final planetary heavy element mass and C/O ratio vary with initial position and to obtain possible formation regions where the planet's final heavy element mass matches observations, we linearly interpolated the simulation results between adjacent data points.

The results of our simulations can provide insight into which regions of the protoplanetary disc a planet is most likely to have originated from based solely off its heavy element content and the chemical composition of the disc. This is illustrated in Fig. 3 for WASP-84b (which has a relatively precise M_Z) and CoRoT-9b (which has an imprecise M_Z); the figure shows the importance of precise observational constraints on the heavy element content for this method. A tight constraint on the heavy element mass leads to a more precise prediction on the origin location

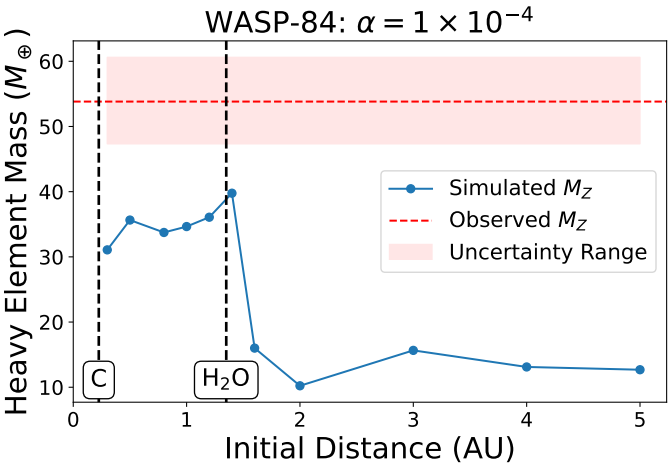

Fig. 4. Heavy element masses of the planet simulated in the disc of WASP-84 for varying initial positions of the planetary embryo in a disc of $\alpha = 1 \times 10^{-4}$ with a refractory carbon content of 20%. The simulated heavy element mass of the planet does not fall within the uncertainty range of observations for any initial position.

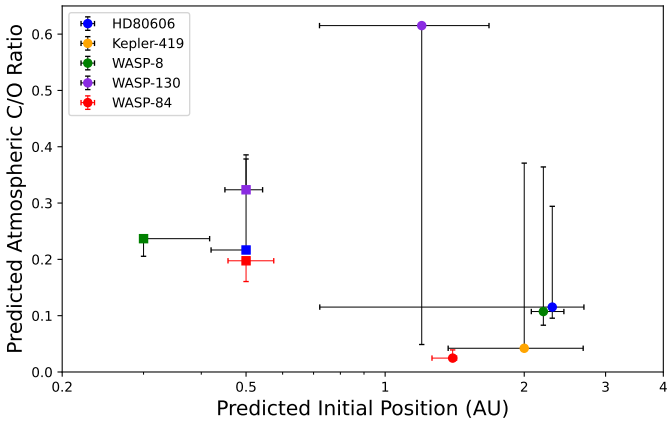

Fig. 5. Predicted initial positions that simulate the observed heavy element masses and the corresponding predicted C/O ratios for the five simulated planets whose heavy element contents were well constrained. All simulations use $\alpha = 1 \times 10^{-4}$. Squares (circles) represent the 'inner' ('outer') formation regions. The points are placed at the initial position that led to the simulations most closely matching the observed heavy element mass. The error bars on the x-axis represent the width of the constrained possible formation regions of each planet, while the error bars on the y-axis show the range in the predicted C/O ratio within each region. WASP-84b is the focus of this work due to its potential observability and is marked with red points and error bars.

of the planet. `Chemcomp` tracks the chemical composition of the growing planet, allowing us to use the inferred origin position to predict properties of the planet's atmosphere. This is illustrated in Fig. 3 for the carbon-to-oxygen ratio of the atmospheres of WASP-84b and CoRoT-9b.

These results show that tighter observational constraints on heavy element mass can significantly improve our ability to infer formation pathways and atmospheric compositions. Our ability to match the observations of Thorngren et al. (2016) depends strongly on the refractory carbon fraction, Fig. 4 shows that the formation of planets with large heavy element contents, such as WASP-84b, cannot be explained if we assume the lower bound of the refractory carbon fraction of 20%. A reduced refractory carbon fraction increases the abundances of CO and CO_2, while decreasing that of H_2O as a larger proportion of the available oxygen is contained in CO and CO_2. Because CO and CO_2 sublimate exterior to the water-ice line, beyond the region where our planets must form to reach the observed enrichment, they cannot contribute significantly to the enrichment of the inner disc gas during early growth. The simultaneous depletion of H_2O further limits the available heavy elements for accretion in the inner disc, compounding this effect. Hence, we did not explore the results of simulations with lower refractory carbon fractions in this work.

Figure 5 shows atmospheric C/O predictions for planets forming in discs with $\alpha = 1 \times 10^{-4}$ whose heavy element contents were well constrained, allowing for tighter constraints to be placed on the formation region and thus the C/O ratio. These constrained formations regions and C/O ratios, along with the inferred final semi-major axes and disc lifetimes, are shown in Table B.1. Planets with uncertainties in their heavy element contents that extended down no lower than to 5% of the total planet mass were identified as being well constrained. Conversely, planets with heavy element measurements with error bars that extended down to almost zero, such as CoRoT-9b, were identified as being poorly constrained as their heavy element content could be explained solely by their core mass. For such planets we can only exclude formation in a small region in the inner disc for which the planet would have accreted too much heavy elements to match observations. In contrast, planets with well-constrained heavy element masses often have two distinct possible formation regions, one in the very inner disc (interior to the water-ice line) and one just beyond the water-ice line. However, as the planet grows it migrates and crosses the water-ice line, allowing it to accrete large fractions of heavy elements (see Appendix B). These 2 formation regions can be seen for WASP-84b and CoRoT-9b in Fig. 3. For both planets, two peaks in the simulated heavy element mass exist; however, the peak in simulated heavy element mass at the H_2O evaporation front is much more pronounced compared to the peak before the C evaporation front for CoRoT-9b than it is for WASP-84b. This can be explained by the abundances in Table A.1. The disc of WASP-84 has a super-solar carbon abundance and a sub-solar oxygen abundance; this leads to a greater heavy element enrichment of the gas at the C evaporation front and a lesser enrichment at the H_2O evaporation front compared to a solar disc because the larger carbon fraction allows more C-grains, as well as more CO and CO_2, to form, which take away oxygen from forming H_2O. The disc of CoRoT-9b has sub-solar carbon and oxygen abundances, with a slightly larger O abundance, leading to a stronger peak in simulated heavy element mass at the H_2O front compared to the C front. The proportion of total planetary mass made up of heavy elements is observed to be approximately 25% for WASP-84b and 7% for CoRoT-9b. These observations can only be explained if WASP-84b formed initially either close to the H_2O front or just beyond the C evaporation front, maximising the simulated metal enrichment. CoRoT-9b's low enrichment can be explained by a large range of formation positions.

There was no inner formation region found for Kepler-419b, it can only accrete the observed amount of heavy elements if it begins to form exterior to the water-ice line due to the timing of material accretion. If a planet grows rapidly in the very inner disc at early times its atmosphere becomes less metal-enriched than if it had formed slightly farther out, beyond the water-ice line, as icy pebbles have not yet drifted inwards and enriched the gas phase. In the inner disc, interior to the water-ice line, refractory solids (silicates and metals) are abundant enough to allow the formation of planet cores of a few Earth masses that can then continue to accrete volatile rich gas. Especially close

to the carbon evaporation line enough vapour exists to push the total heavy element content of the planet growing there into the regime of WASP-84b.

3.2. Impact of model assumptions

3.2.1. Fragmentation velocity

The grain fragmentation velocity sets the size of the pebbles in the inner disc region, where their size is dominated by fragmentation rather than by drift, which dominates the pebble sizes in the outer disc regions. We used here a fixed fragmentation velocity of 5m/s. Using a lower fragmentation velocity of 1m/s would reduce the grain size by a factor of 25 (Birnstiel et al. 2012). As such, the pebbles would drift more slowly; however, they would still remain very large and would be able to significantly enrich the inner disc with vapour (Bitsch & Mah 2023). The enrichment with heavy elements in the inner disc regions is determined by two effects: the inward drifting velocity of the pebbles that set how fast the inner disc gets enriched (between 0.5 and 1.0 Myr), while the disc's viscosity sets how long the inner disc can stay enriched, because the viscosity determines the inward velocity of the gas. In particular, the low viscosity that allows us to match the heavy element content of WASP-84b, results in a long enrichment of the vapour phase of the inner disc independently of the grain fragmentation velocity (see Bitsch & Mah 2023). We thus think that the effects of the grain fragmentation velocity are minimal for the mechanism that we propose to constrain the formation location of giant planets via their total heavy element content.

Interior to the water-ice line, the pebbles lose their icy component, resulting in smaller pebble sizes with Stokes numbers of the order of 10^{-3} to 10^{-2} for low fragmentation velocities of 1 m/s and up to a factor of 100 larger if the fragmentation velocity is increased to 10m/s (e.g. Bitsch & Mah 2023). The low Stokes numbers are sometimes associated with difficulties in building cores via pebble accretion in these regions (e.g. Batygin & Morbidelli 2023); the formation of planetesimals via the streaming instabilities at these low Stokes numbers is also difficult (e.g. Li & Youdin 2021). If the planets grow via pebble accretion, their final mass is set by the pebble isolation mass, which scales strongly with the disc's aspect ratio (e.g. Lambrechts et al. 2014; Bitsch et al. 2018). However, at low Stokes numbers, the disc might be hotter due to the increased opacity of the large grains compared to the small grains, resulting in aspect ratios high enough to form cores capable of accreting gas (e.g. Savvidou & Bitsch 2021), if they can grow efficiently enough. In reality, probably a mixture of growth mechanism (pebble accretion, planetesimal accretion, collision between growing embryos) needs to operate to allow cores to grow massive enough to accrete a gaseous envelope and transition into gas giants. This process is not modelled here in detail and also generally not fully understood. However, our study shows that if cores form in these inner disc regions, they will accrete a large fraction of heavy elements via the gas, allowing them to match the large heavy element content of the observed giant planets, independently of how the cores reached masses large enough to allow efficient gas accretion.

3.2.2. Initial embryo formation time and mass

Planetary embryos below the so-called pebble transition mass accrete in the slow Bondi regime, while planets above the pebble transition mass accrete in the Hill regime (Lambrechts & Johansen 2012; Johansen & Lambrechts 2017). If we were to start our embryos at a lower mass, they would need a longer time to grow. Essentially, it means we could mimic this effect by putting embryos of the same mass at later times. However, if planetary embryos are inserted at later times, most of the pebbles have already drifted inwards, preventing their growth into gas giants (Savvidou & Bitsch 2023). In order to form giant planets, we thus require an early planetary embryo insertion time.

4. Discussion and conclusions

Formation location and migration history influence not only the total heavy element content of a planet but also its atmospheric carbon-to-oxygen (C/O) ratio (Öberg et al. 2011; Madhusudhan et al. 2014; Turrini et al. 2021; Bitsch et al. 2022; Penzlin et al. 2024). As planets migrate through chemically distinct regions, they accrete gas with varying C and O abundances. For example, accretion inside the water-ice line results in oxygen-rich gas, lowering the C/O ratio, while accretion beyond this line yields higher C/O ratios.

Because `Chemcomp` tracks elemental abundances, we can also predict the C/O ratio for each formation location. Combining these C/O values with the constrained formation regions provides predicted ranges for each planet's atmospheric composition (the minimum to maximum C/O within the constrained formation region). Figure 3 shows how both the final heavy element mass and the atmospheric C/O ratio of the planet change with initial position. For both planets there are two constrained regions where the linear interpolation of the simulated heavy element mass is within the uncertainty range. So we have two predicted ranges for the C/O ratio of each planet that correspond to the range in simulated C/O values within each region.

The range of predicted C/O depends on how well the planet's initial position is constrained: for planets with poorly measured heavy element masses, this range is wider. Figure 3 illustrates this for CoRoT-9b, whose poorly constrained heavy element mass results in a large range of possible formation locations and therefore a broad predicted C/O range.

We have demonstrated how the carbon-to-oxygen ratio of the planetary atmosphere could be predicted for planets whose formation location is constrained via their total heavy element content. We can also make predictions about the other chemical elements used in our simulations. Appendix D shows the O/H and C/H predictions for WASP-84b and CoRoT-9b. In Table 1 we summarise these findings and include predictions of Mg, Si, S, and Fe within the atmosphere of WASP-84b for both its inner and outer formation regions, giving additional constraints for observations. The predicted O/H enrichment compared to the host star is dominated by water, which is accreted by the growing planet interior to the H_2O evaporation front, while the high C/H enrichment in the inner formation region is due to carbon grains, which can be accreted into the atmosphere when the planet moves interior to the C evaporation front. The high sulphur abundance compared to other refractories is due to the evaporation of H_2S, which is trapped in water ice (Santos et al. 2025), at the H_2O evaporation front, enriching the gas in the inner disc with sulphur. H_2S is also enhanced compared to a solar composition due to the slightly super-solar S abundance of WASP-84.

By calculating the transmission spectroscopy metric (TSM; see Kempton et al. 2018) of the planets in the sample with well-constrained heavy element contents, we identified WASP-84b as a prime target for atmospheric characterisation (this is described

Table 1. WASP-84b predicted atmospheric abundances for the inner and outer formation regions.

Region	Element	Minimum		Maximum		Best Match	
		Number ratio	Normalised ratio	Number ratio	Normalised ratio	Number ratio	Normalised ratio
Inner	C/O	0.161	0.252	0.197	0.308	0.197	0.308
	C/H	3.05×10^{-3}	10.45	3.77×10^{-3}	12.89	3.77×10^{-3}	12.89
	O/H	1.85×10^{-2}	40.50	1.91×10^{-2}	41.72	1.91×10^{-2}	41.72
	Mg/H	1.06×10^{-5}	0.26	1.1×10^{-5}	0.27	1.1×10^{-5}	0.27
	Si/H	9.74×10^{-6}	0.26	1.01×10^{-5}	0.27	1.01×10^{-5}	0.27
	S/H	1.41×10^{-4}	9.20	1.47×10^{-4}	9.54	1.47×10^{-4}	9.54
	Fe/H	9.46×10^{-6}	0.27	9.72×10^{-6}	0.27	9.72×10^{-6}	0.27
Outer	C/O	0.025	0.039	0.039	0.061	0.025	0.039
	C/H	5.76×10^{-4}	1.97	7.42×10^{-4}	2.94	5.76×10^{-4}	1.98
	O/H	2.05×10^{-2}	44.84	2.34×10^{-2}	51.18	2.34×10^{-2}	51.18
	Mg/H	6.08×10^{-6}	0.15	7.9×10^{-6}	0.19	6.08×10^{-6}	0.15
	Si/H	5.58×10^{-6}	0.15	7.25×10^{-6}	0.19	5.58×10^{-6}	0.15
	S/H	1.57×10^{-4}	10.21	1.82×10^{-4}	11.85	1.82×10^{-4}	11.85
	Fe/H	5.25×10^{-6}	0.15	6.82×10^{-6}	0.19	5.25×10^{-6}	0.15

Notes. For each element, Number Ratio is the absolute number ratio, and Normalised Ratio is the value normalised to the host star's abundance. The minimum and maximum values correspond to the range within the constrained region, and the best match is the ratio at the data point that most closely matches the heavy element content of WASP-84b.

in Appendix C). This provides a means of testing the concept put forward in this paper.

The recent observations of WASP-121b's atmosphere revealed an atmosphere highly enriched in carbon, oxygen, and silicon (Evans-Soma et al. 2025), which can be explained by the accretion of gas enriched in these elements. Our simulations for WASP-84b show similar predicted enrichments for oxygen and carbon, but not for silicon. This could be attributed to the fact that WASP-121b accreted most of its mass even closer to the host star, where the rock-forming species also evaporate and are accreted via the gas. WASP-121b orbits with a period of 1.3 days. While such an ultra-short period may result from tidal interaction with the central star followed by planet-planet scattering rather than pure disc-driven migration, migration may still have brought the planet close to the star before such events occurred. In this case, the heavy element accretion could be aided by the mechanisms that we investigated in this work. While other mechanisms such as the late accretion of dust, comets, or planetesimals may contribute to the observed enrichment (e.g. Arras et al. 2022; Morbidelli et al. 2023; Bitsch & Mah 2023; Seligman et al. 2022; Shibata & Helled 2024), planetesimal accretion alone is unlikely to explain the high heavy element content. In fact, efficient planetesimal formation generally reduces the heavy-element fraction of forming giant planets, as planetesimal accretion is less efficient than the accretion of vapour-enriched gas (Danti et al. 2023). Putting this together, the high total heavy element content of giant planets implies a high enrichment of the atmosphere, especially in carbon and oxygen, which is explained within our model. This offers a testable prediction of the pebble drift and evaporation model.

Our model is also consistent with new results regarding WASP-80b's composition (Acuña-Aguirre et al. 2026) with respect to the heavy element content, C/O, and core mass. The method described in this paper requires stellar elemental abundances as an input for our formation model, which are not available for WASP-80, and so we cannot derive a definite formation location for the planet. To confirm the general consistency of our model with the results of Acuña-Aguirre et al. (2026), we estimated the stellar abundances of WASP-80 according to the scaling relation of Bitsch & Battistini (2020), for which only the [Fe/H] of WASP-80 (Terrien et al. 2015) is required as an input. Bardet et al. (2025) present atmospheric C/O ratio retrievals for ten hot Jupiters based on JWST transmission spectra. Their findings show that the retrieved C/O values mostly lie between ~0.1 and 0.6, with median values concentrated in the range 0.2–0.4. These observationally derived values fall within the same broad range as the predicted atmospheric C/O ratios shown in Fig. 5. Although the planets analysed by Bardet et al. (2025) are different from those modelled here, the overlap in C/O ranges highlights the plausibility of our predictions and the need for follow-up observations to verify the efficacy of the methods put forward in this paper for determining the birthplaces of exoplanets based off their heavy element content.

Acknowledgements. Barry O'Donovan acknowledges the support of the European Research Council (ERC) Starting Grant (ExoPEA: 01164652). We thank the referee for the comments that helped to improve this work.

References

Acuña-Aguirre, L., Kreidberg, L., Mollière, P., & Bachmann, N. 2026, A&A, in press, https://doi.org/10.1051/0004-6361/202556519
Agnew, M. T., Maddison, S. T., Horner, J., & Kane, S. R. 2019, MNRAS, 485, 4703
Altwegg, K., Balsiger, H., Hänni, N., et al. 2020, NatAstron, 4, 533
Andama, G., Mah, J., & Bitsch, B. 2024, A&A, 683, A118
Armitage, P. J. 2013, Astrophyics of Planet Formation CUP
Arras, P., Wilson, M., & Pryal, Matthew Baker, J. 2022, ApJ, 932, 90
Asplund, M., Grevesse, N., Sauval, A. J., & Scott, P. 2009, ARA&A, 47, 481
Ataiee, S., Baruteau, C., Alibert, Y., & Benz, W. 2018, A&A, 615, A110
August, P. C., Bean, J. L., Zhang, M., & Lunine, J. 2023, ApJ, 953, L24
Baraffe, I., Homeier, D., Allard, F., & Chabrier, G. 2015, A&A, 577, A42
Bardet, D., Changeat, Q., Venot, O., & Panek, E. 2025, A&A, 699, A342
Batygin, K., & Morbidelli, A. 2023, Nature, 7, 330
Bean, J. L., Xue, Q., August, P. C., et al. 2023, Nature, 618, 43
Beaugé, C., & Nesvorný, D. 2012, ApJ, 751, 119
Bell, K. R., Cassen, P. M., Klahr, H. H., & Henning, T. 1997, ApJ, 486, 372

Benítez-Llambay, P., Masset, F., Koenigsberger, G., & Szulágyi, J. 2015, Nature, 520, 63
Bergin, E. A., Blake, G. A., Ciesla, F., Hirschmann, M. M., & Li, J. 2015, Proc. Natl. Acad. Sci. U.S.A., 112, 29
Birnstiel, T., Klahr, H., & Ercolano, B. 2012, A&A, 539, A148
Bitsch, B., & Battistini, C. 2020, A&A, 633, A10
Bitsch, B., & Izidoro, A. 2023, A&A, 674, A178
Bitsch, B., & Mah, J. 2023, A&A, 679, A11
Bitsch, B., Crida, A., Morbidelli, A., Kley, W., & Dobbs-Dixon, I. 2013, A&A, 549, A124
Bitsch, B., Morbidelli, A., Johansen, A., et al. 2018, A&A, 612, A30
Bitsch, B., Trifonov, T., & Izidoro, A. 2020, A&A, 643, A66
Bitsch, B., Schneider, A. D., & Kreidberg, L. 2022, A&A, 665, A138
Bloot, S., Miguel, Y., Bazot, M., & Howard, S. 2023, MNRAS, 523, 6282
Booth, R. A., & Ilee, J. D. 2017, MNRAS, 487, 3, 3998
Booth, R. A., Clarke, C. J., & Madhusudhan, Nikku Ilee, J. D. 2017, MNRAS, 469, 3994
Chatterjee, S., Ford, E. B., Matsumura, S., & Rasio, F. A. 2008, ApJ, 686, 580
Chen, Y. Q., Nissen, P. E., Zhao, G., & Asplund, M. 2002, A&A, 390, 225
Danti, C., Bitsch, B., & Mah, J. 2023, A&A, 679, L7
Dawson, R. I., & Johnson, J. A. 2018, ARA&A, 56, 175
Denman, T. R., Leinhardt, Z. M., Carter, P. J., & Mordasini, C. 2020, MNRAS, 496, 2, 1166
Eberlein, M., Bitsch, B., & Helled, R. 2024, A&A, 691, A50
Evans-Soma, T. M., Sing, David K. Barstow, J. K., & Piette, A. A. A. 2025, Nat. Astron., 9, 845
Flock, M., Turner, N. J., Mulders, G. D., et al. 2019, A&A, 630, A147
Georgakarakos, N., Eggl, S., & Dobbs-Dixon, I. 2018, ApJ, 856, 155
Güdel, M., Briggs, K. R., Arzner, K., et al. 2007, A&A, 468, 2, 353
Haworth, T. J., Clarke, C. J., Rahman, W., Winter, A. J., & Facchini, S. 2018, MNRAS, 481, 1, 452
Haworth, T. J., Coleman, G. A. L., Qiao, L., Sellek, A. D., & Askari, K. 2023, MNRAS, 526, 4315
Houge, A., Johansen, A., Bergin, E., & Ciesla, F. J. 2025, A&A, 699, A227
Hühn, L. A., & Bitsch, B. 2023, MNRAS, 676, A87
Johansen, A., & Lambrechts, M. 2017, Annu. Rev. Earth Planet. Sci., 45, 359
Kempton, E. M.-R., Bean, J. L., Louie, D. R., et al. 2018, PASP, 130, 993
Kreidberg, L., Bean, J. L., Désert, J.-M., et al. 2014, ApJ, 793, L27
Lambrechts, M., & Johansen, A. 2012, A&A, 544, A32
Lambrechts, M., Johansen, A., & Morbidelli, A. 2014, A&A, 532, A35
Laughlin, G., Deming, D., Langton, J., et al. 2009, Nature, 457, 562
Li, R., & Youdin, A. N. 2021, ApJ, 919, 107
Lodders, K. 2003, ApJ, 591, 1220
Louden, T., Wheatley, P. J., & Briggs, K. 2017, MNRAS, 464, 2396
Louie, D. R., Deming, D., Albert, L., et al. 2018, PASP, 130, 044401
Lueber, A., Novais, A., Fisher, C., & Heng, K. 2024, A&A, 687, A110
Lynden-Bell, D., & Pringle, J. E. 1974, MNRAS, 168, 603
Madhusudhan, N., Amin, M. A., & Kennedy, G. M. 2014, ApJ, 794, L12
Madhusudhan, N., Bitsch, B., Johansen, A., & Eriksson, L. 2017, MNRAS, 469, 4102
Mah, J., Bitsch, B., Pascucci, I., & Henning, T. 2023, A&A, 677, L7
Mamajek, E. E. 2009, AIP Conf. Proc., 1158, 3
Mollière, P., Molyarova, T., Bitsch, B., et al. 2022, ApJ, 934, 74
Morbidelli, A., Batygin, K., & Lega, E. 2023, A&A, 675, A75
Mordasini, C., Alibert, Y., Benz, W., Klahr, H., & Henning, T. 2012, A&A, 541, A97
Öberg, K. I., Murray-Clay, R., & Bergin, E. A. 2011, ApJ, 743, L16
Ogihara, M., Hori, Y., Kunitomo, M., & Kurosaki, K. 2021, MNRAS, 648, L1
Ohno, K., Ikoma, M., Okuzumi, S., & Kimura, T. 2025, PASJ, submitted [arXiv:2506.16060]
Ormel, C. W., & Klahr, H. H. 2010, A&A, 520, A43
Owen, J. E., Ercolano, B., & Clarke, C. J. 2011, MNRAS, 412, 13
Paardekooper, S. J. 2014, MNRAS, 444, 2031
Paardekooper, S.-J., & Johansen, A. 2018, Space Sci. Rev., 214, 38
Paardekooper, S. J., Baruteau, C., & Kley, W. 2011, MNRAS, 410, 293
Peerani, L., Howard, S., & Helled, R. 2026, A&A, in press, https://doi.org/10.1051/0004-6361/202557645
Penzlin, A. B. T., Booth, R. A., Kirk, J., & Owen, J. E. 2024, MNRAS, 535, 171
Pfalzner, S., Dehghani, S., & Michel, A. 2022, ApJ, 939, L10
Picogna, G., Ercolano, B., & Espaillat, C. C. 2021, MNRAS, 508, 3611
Pollack, J. B., Hubickyj, O., Bodenheimer, P., et al. 1996, Icarus, 124, 62
Powell, D., Feinstein, A. D., Lee, E. K. H., et al. 2024, Nature, 626, 979
Pringle, J. E. 1981, ARA&A, 19, 137
Santos, J. C., Piacentino, E. L., Bergner, J. B., Rajappan, M., & Öberg, K. I. 2025, A&A, 698, A254
Savvidou, S., & Bitsch, B. 2021, A&A, 650, A132
Savvidou, S., & Bitsch, B. 2023, A&A, 679, A42
Schlecker, M., Mordasini, C., Emsenhuber, A., & Klahr, H. 2021, A&A, 656, A71
Schneider, A. D., & Bitsch, B. 2021, A&A, 654, A71
Seligman, D. Z., Becker, J., Adams, F. C., Feinstein, A. D., & Rogers, L. A. 2022, ApJ, 933, L7
Shakura, N. I., & Sunyaev, R. A. 1973, A&A, 24, 337
Shibata, S., & Helled, R. 2024, A&A, 689, A26
Taylor, J., Radica, M., Welbanks, L., et al. 2023, MNRAS, 524, 1
Terrien, R. C., Mahadevan, S., Deshpande, R., & Bender, C. F. 2015, ApJS, 220, 16
Teske, J. K., Thorngren, D. P., Fortney, J. J., Hinkel, N. R., & Lopez, E. D. 2019, ApJ, 158, 239
Thorngren, D. P., Fortney, J. J., Murray-Clay, R. A., & Lopez, E. D. 2016, ApJ, 831, 64
Turrini, D., Schisano, E., Fonte, S., & Molinari, S. 2021, ApJ, 909, 40
Vazan, A., Helled, R., & Guillot, T. 2018, A&A, 610, L14
Venturini, J., & Helled, R. 2020, A&A, 634, A31
Winn, J. N., & Fabrycky, D. C. 2015, ARA&A, 53, 409

Appendix A: Stellar abundances

Table A.1 shows all the stars from the Teske et al. (2019) dataset along with their stellar abundances, our calculated DTG ratios, stellar masses and the total planetary mass and planetary heavy element mass of the corresponding planet from the Thorngren et al. (2016) dataset. As explained in Sect. 2, we simulated the formation only of those planets that are above $0.5 M_J$. Table A.1 thus only includes the stars from the Teske et al. (2019) dataset that hosted planets above this threshold mass.

Table A.1. Stellar abundances (Teske et al. 2019), computed DTGs, stellar masses, planetary masses, and planetary heavy element masses for each disc simulated in this work.

Star	[C/H]	[O/H]	[Mg/H]	[Si/H]	[Fe/H]	DTG	Mass ($M_\odot$)	Planet Mass (M_J)	M_Z ($M_\oplus$)
HD80606	0.270	0.200	0.328	0.328	0.28	2.669×10^{-2}	1.05	3.94 ± 0.11	$215.69^{+52.63}_{-52.23}$
Kepler-432	-0.103	-0.085	0.005	0.070	0.02	1.338×10^{-2}	1.35	5.84 ± 0.05	$67.39^{+60.95}_{-67.29}$
Kepler-419	0.131	0.131	0.010	0.117	0.03	1.959×10^{-2}	1.39	2.50 ± 0.30	$198.16^{+126.80}_{-100.72}$
WASP-8	0.149	0.153	0.250	0.273	0.29	2.335×10^{-2}	0.99	$2.24^{+0.08}_{-0.09}$	$84.34^{+43.33}_{-38.00}$
HAT-P-15	0.182	0.118	0.212	0.265	0.27	2.251×10^{-2}	1.01	1.95 ± 0.07	$42.45^{+30.67}_{-42.35}$
WASP-130	0.274	0.179	0.269	0.322	0.29	2.593×10^{-2}	1.04	1.23 ± 0.04	$108.83^{+17.58}_{-17.35}$
Kepler-539	-0.188	-0.047	-0.040	-0.099	-0.10	1.247×10^{-2}	1.05	0.97 ± 0.29	$154.94^{+51.90}_{-48.76}$
CoRoT-9	-0.111	-0.041	0.007	-0.028	-0.02	1.355×10^{-2}	0.96	0.84 ± 0.07	$18.87^{+13.30}_{-18.77}$
WASP-84	0.036	-0.030	0.014	0.066	0.05	1.535×10^{-2}	0.84	0.69 ± 0.03	$53.82^{+6.79}_{-6.48}$
HAT-P-17	0.053	0.019	0.062	0.060	0.02	1.633×10^{-2}	0.86	0.53 ± 0.02	$14.08^{+6.56}_{-6.24}$

Appendix B: Planet semi-major axis evolution and the effects of varying viscosity

Figure B.1 shows the semi-major axis evolution of the planets that accreted the observed amount of heavy elements for the 3 different viscosities simulated in the discs of WASP-84 and CoRoT-9. The heavy element content in the gas phase in the protoplanetary disc is plotted as a colour map, with darker blue indicating more heavy-element enrichment. The evaporation fronts of C, H_2O and CO_2 are also plotted. `Chemcomp` stops migration planet migration at 0.2AU just before the inner edge of the disc grid as grid cells interior to the planet's position are required to calculate the gradients needed to compute the planet's migration and gap opening. Physically this can be justified by the existence of a migration trap in the inner disc halting the planet's migration (e.g. Flock et al. 2019). For some planets and viscosities (e.g. both CoRoT-9b and WASP-84b at $\alpha = 5 \times 10^{-4}$ and $\alpha = 1 \times 10^{-4}$) there are 2 possible formation regions that lead to the planet accreting the observed amount of heavy elements, Fig. 3 illustrates this for CoRoT-9b and WASP-84b at $\alpha = 1 \times 10^{-4}$ and Fig. B.2 does so for $\alpha = 5 \times 10^{-4}$. These tracks demonstrate that although outer planets begin in less metal-enriched regions, they migrate into the inner disc closer to the water-ice line, where the initial increase with vapour is largest, allowing them to become enriched in heavy elements. An $\alpha = 1 \times 10^{-3}$ disc fails to reproduce the observed heavy element enrichment of WASP-84b for all initial positions, this is illustrated further in Fig. B.2. In general high α discs ($\alpha = 5 \times 10^{-4}$ and $\alpha = 1 \times 10^{-3}$) often result in very rapid growth in the early stages of the disc ($\lesssim 1$ Myr). At the same time, the enrichment of the disc with heavy elements is not large enough to explain the heavy element contents of the giant planets. For example, WASP-84b has roughly a heavy element content of 25% of its mass, but the discs with high viscosity do not reach enrichments of heavy elements larger than 10%. In addition, we stopped the simulations when the planet reached its observed mass; this required the disc to disperse in unrealistically short timescales. For this reason we focus on the $\alpha = 1 \times 10^{-4}$ simulations in this paper. However, for completeness the simulated C/O of WASP-84b is plotted as a function of initial position for WASP-84b in discs of $\alpha = 5 \times 10^{-4}$ and $\alpha = 1 \times 10^{-3}$ in Fig. B.3. It is important to note that there is no constrained region and thus no predicted C/O ratio for the $\alpha = 1 \times 10^{-3}$ case as we are unable to match the observed heavy element mass of WASP-84b at this viscosity.

Table B.1. Constrained initial planetary embryo semi-major axes, final semi-major axes (i.e. the planet's position when it reaches its observed mass), C/O number ratios, and disc lifetimes for an $\alpha = 10^{-4}$ disc.

Planet	Region	Initial a_p (AU)	Final a_p (AU)	C/O (Number Ratio)	Disc Lifetime (Myr)
HD80606b	Inner	$0.5_{-0.08}$	0.2	$0.22^{+0.16}$	$4.48^{+3.06}$
	Outer	$2.3^{+0.39}_{-1.58}$	$0.39^{+0.29}_{-0.19}$	$0.12^{+0.18}_{-0.02}$	$5.56^{+0.16}_{-0.99}$
Kepler-419b	Inner	-	-	-	-
	Outer	$2.0^{+0.68}_{-0.63}$	$0.53^{+0.53}_{-0.21}$	$0.042^{+0.33}$	$4.17^{+7.12}$
WASP-8b	Inner	$0.3^{+0.12}$	0.2	$0.24_{-0.03}$	$7.08_{-2.29}$
	Outer	$2.2^{+0.24}_{-0.13}$	$0.88^{+0.21}_{-0.07}$	$0.11^{+0.26}_{-0.02}$	$3.52^{+0.06}_{-0.18}$
WASP-130b	Inner	$0.5^{+0.04}_{-0.05}$	0.2	$0.32^{+0.04}$	$1.18^{+0.71}_{-0.03}$
	Outer	$1.2^{+0.48}_{-0.48}$	$0.2^{+0.85}$	$0.62_{-0.57}$	$3.3_{-1.55}$
WASP-84b	Inner	$0.5^{+0.07}_{-0.04}$	0.2	$0.2^{-0.04}$	$1.91^{+0.11}$
	Outer	$1.4^{+0.03}_{-0.14}$	$0.94^{+0.02}_{-0.44}$	$0.03^{+0.01}$	$1.13^{+0.56}$

Notes. The final semi-major axis is defined as the planet's position when it reaches its observed mass in the simulation. Shown are the values for the simulation that most closely matched the observed heavy element mass with the uncertainties corresponding to the range of these quantities within the constrained formation regions (all quantities are linearly interpolated between each simulation data point). There is no constrained inner formation region for Kepler-419b.

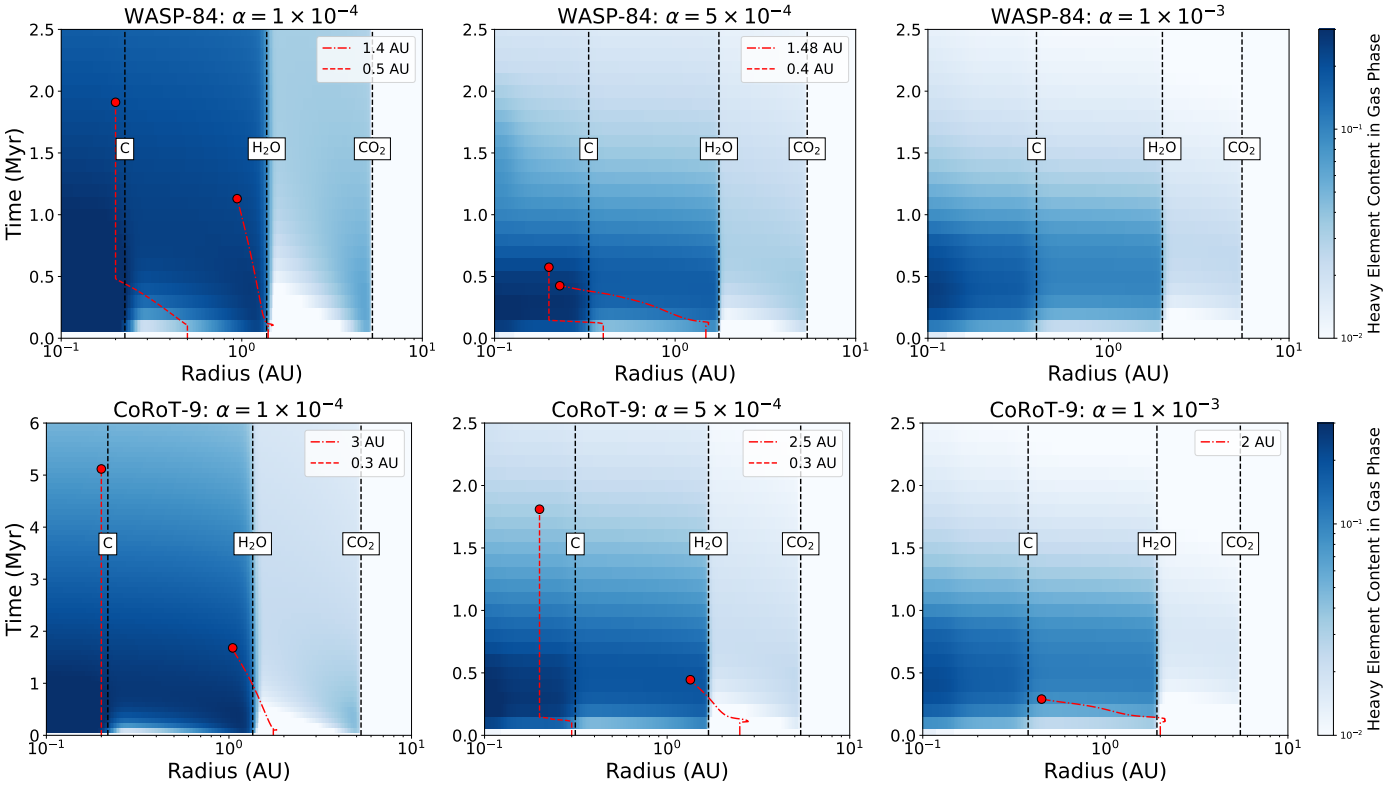

Fig. B.1. Semi-major axis evolutions of planets forming in the disc of WASP-84 (*top*) and CoRoT-9 (*bottom*) for discs of different viscosities: $\alpha = 1 \times 10^{-4}$ (*left*), $\alpha = 5 \times 10^{-4}$ (*middle*), and $\alpha = 1 \times 10^{-3}$ (*right*). Red circles indicate the time and position at which the planet reached its observed mass for each simulation. All plotted evolutions are for simulations that matched the observed heavy element masses of WASP-84b and CoRoT-9b. In the disc of WASP-84, for $\alpha = 1 \times 10^{-3}$, the observed heavy element mass could not be matched by simulations for any initial position.

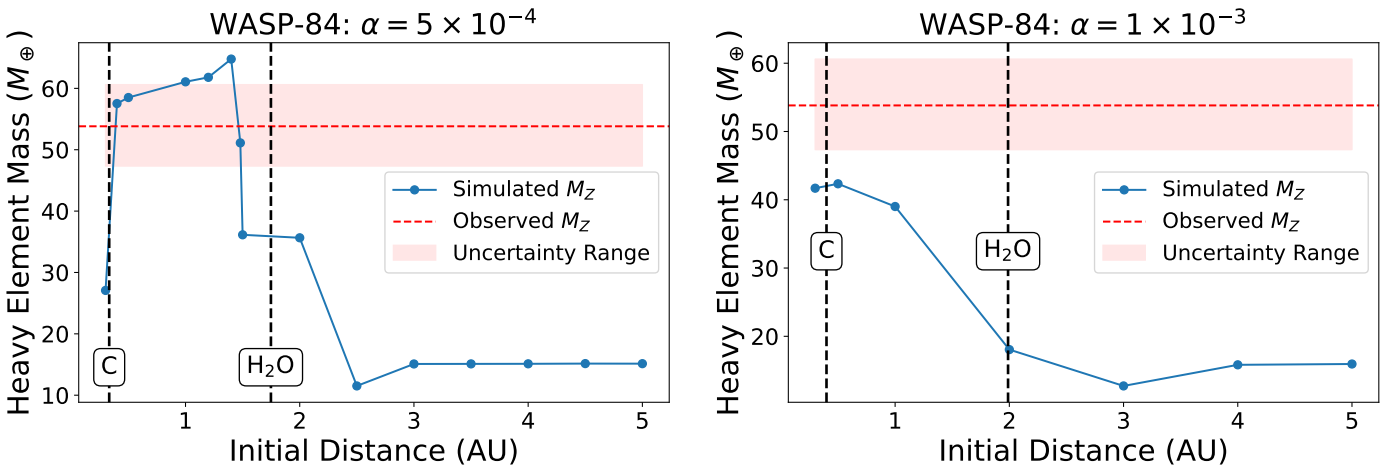

Fig. B.2. Heavy element masses of the planet simulated in the disc of WASP-84 for varying initial positions of the planetary embryo in a disc of $\alpha = 5 \times 10^{-4}$ (*left*) and in a disc of $\alpha = 1 \times 10^{-3}$ (*right*). The simulated heavy element mass of the planet in the $\alpha = 1 \times 10^{-3}$ disc does not fall within the uncertainty range of observations for any initial position, whereas the $\alpha = 5 \times 10^{-4}$ disc has two separate possible formation regions, like the $\alpha = 1 \times 10^{-4}$ disc (see Fig. 3).

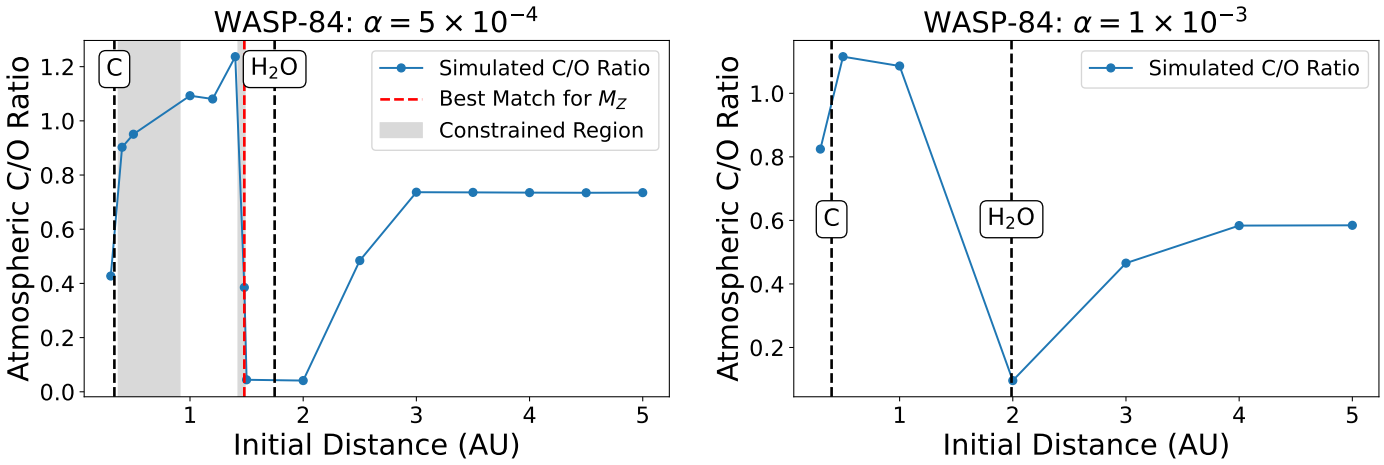

Fig. B.3. Predicted atmospheric C/O number ratios of the planet simulated in the disc of WASP-84 as a function of initial position for a disc of $\alpha = 5 \times 10^{-4}$ (*left*) and $\alpha = 1 \times 10^{-3}$ (*right*). The dashed red line shows the best-fit formation location based on the heavy element mass, and the grey region indicates the constrained range of possible formation locations. H_2O and C evaporation fronts are shown as dashed black lines in all panels. No possible formation regions were identified for WASP-84b in a disc of $\alpha = 1 \times 10^{-3}$.

Appendix C: TSM calculation

Kempton et al. (2018) present a framework for quantifying how amenable an exoplanet is to atmospheric characterisation. The TSM, which is proportional to the expected transmission spectroscopy signal to noise ratio, was calculated as follows:

$$\mathrm{TSM} = (\text{scale factor}) \times \frac{R_p^3 T_{eq}}{M_p R_*^2} \times 10^{-m_J/5}. \tag{C.1}$$

The quantities in Eq. C.1 are defined as follows:

1. R_p is the radius of the planet in units of Earth radii.
2. M_p is the mass of the planet in units of Earth masses.
3. $R_\star$ is the radius of the host star in units of solar radii.
4. $T_{\rm eq}$ is the planet's equilibrium temperature in Kelvin calculated for zero albedo and full day-night heat redistribution according to

$$T_{\rm eq} = T_\star \sqrt{\frac{R_\star}{a}} \left(\frac{1}{4}\right)^{1/4}, \tag{C.2}$$

   where $T_\star$ is the host star effective temperature in Kelvin, and a is the orbital semi-major axis given in the same units as $R_\star$.
5. m_J is the apparent magnitude of the host star in the J band.

The 'scale factor' in Eq. C.1 is a normalisation constant selected to give one-to-one scaling between the analytic transmission metric of Kempton et al. (2018) and the more detailed work of Louie et al. (2018). Kempton et al. (2018) calculates the scale factor separately for each planet radius bin, their sample uses radial bins up to $R_p < 10R_\oplus$. Since the planets we wished to calculate the TSM for (HD80606b, Kepler-419b, WASP-8b, WASP-130b, and WASP-84b) have radii of between $10R_\oplus$ and $12.7R_\oplus$, we used the scale factor of 1.15 calculated for the upper most radial bin in Kempton et al. (2018).

Table C.1. TSM values for selected giant exoplanets.

Planet	TSM
HD 80606b	14.7
Kepler-419b	1.4
WASP-8b	55.6
WASP-84b	115.9
WASP-130b	22.5

Notes. TSM values are calculated following Kempton et al. (2018). Values needed to calculate TSM were obtained from the NASA Exoplanet Archive.

The TSM values presented in Table C.1 provide a means of assessing the relative suitability of the selected planets for atmospheric characterisation via transmission spectroscopy. Kempton et al. (2018) propose a TSM threshold of ~90 for giant planets ($4 < R_p < 10\,R_\oplus$) to identify high-priority targets for JWST/NIRISS observations. While this guideline does not strictly extend to planets with radii exceeding $10\,R_\oplus$, it remains a useful benchmark. Of the planets considered here, WASP-84b stands out with a TSM of 115.9, exceeding the recommended threshold and indicating strong potential for atmospheric follow-up. WASP-8b also shows a moderately high TSM (55.6), suggesting some potential suitability. For completeness, the predicted atmospheric abundances for WASP-8b are shown in Table C.2. In contrast, HD 80606b, WASP-130b, and Kepler-419b have significantly lower TSM values (14.7, 22.5, and 1.4, respectively), implying a low transmission signal-to-noise. Notably, HD 80606b, despite its high mass and large radius, is known for its extreme orbital eccentricity (Laughlin et al. 2009), which may complicate atmospheric observations and their interpretation. These results reinforce the utility of the TSM as a prioritisation tool, as demonstrated in the validation work of Louie et al. (2018), and support the selection of WASP-84b as a strong candidate for atmospheric spectroscopy to test our formation theory.

Table C.2. Predicted WASP-8b atmospheric abundances for the inner and outer formation regions.

Region	Element	Minimum		Maximum		Best Match	
		Number Ratio	Normalised Ratio	Number Ratio	Normalised Ratio	Number Ratio	Normalised Ratio
Inner	C/O	0.205	0.377	0.237	0.436	0.237	0.436
	C/H	1.43×10^{-3}	3.77	3.0×10^{-3}	7.92	1.43×10^{-3}	3.77
	O/H	6.04×10^{-3}	8.67	1.56×10^{-2}	22.45	6.04×10^{-3}	8.67
	Mg/H	1.18×10^{-6}	0.02	2.76×10^{-6}	0.04	1.18×10^{-6}	0.02
	Si/H	1.01×10^{-6}	0.02	2.37×10^{-6}	0.04	1.01×10^{-6}	0.02
	S/H	4.9×10^{-5}	1.98	2.41×10^{-4}	9.75	4.9×10^{-5}	1.98
	Fe/H	1.62×10^{-5}	0.26	1.3×10^{-4}	2.11	1.62×10^{-5}	0.26
Outer	C/O	0.083	0.153	0.402	0.739	0.107	0.197
	C/H	1.31×10^{-3}	3.45	1.43×10^{-3}	3.78	1.34×10^{-3}	3.55
	O/H	3.56×10^{-3}	5.10	1.64×10^{-2}	23.54	1.25×10^{-2}	17.96
	Mg/H	3.91×10^{-6}	0.06	4.03×10^{-6}	0.06	4.03×10^{-6}	0.06
	Si/H	3.35×10^{-6}	0.06	3.46×10^{-6}	0.06	3.46×10^{-6}	0.06
	S/H	1.3×10^{-5}	0.53	1.19×10^{-4}	4.81	8.58×10^{-5}	3.47
	Fe/H	3.4×10^{-6}	0.06	3.51×10^{-6}	0.06	3.51×10^{-6}	0.06

Appendix D: Oxygen and carbon abundances

Similarly to Fig. 3, Fig. D.1 shows how the atmospheric O/H and C/H ratios change with the initial position of the planetary embryo. Once again, a good constraint on the heavy element content is essential for obtaining precise predictions of the atmospheric properties of the planet.

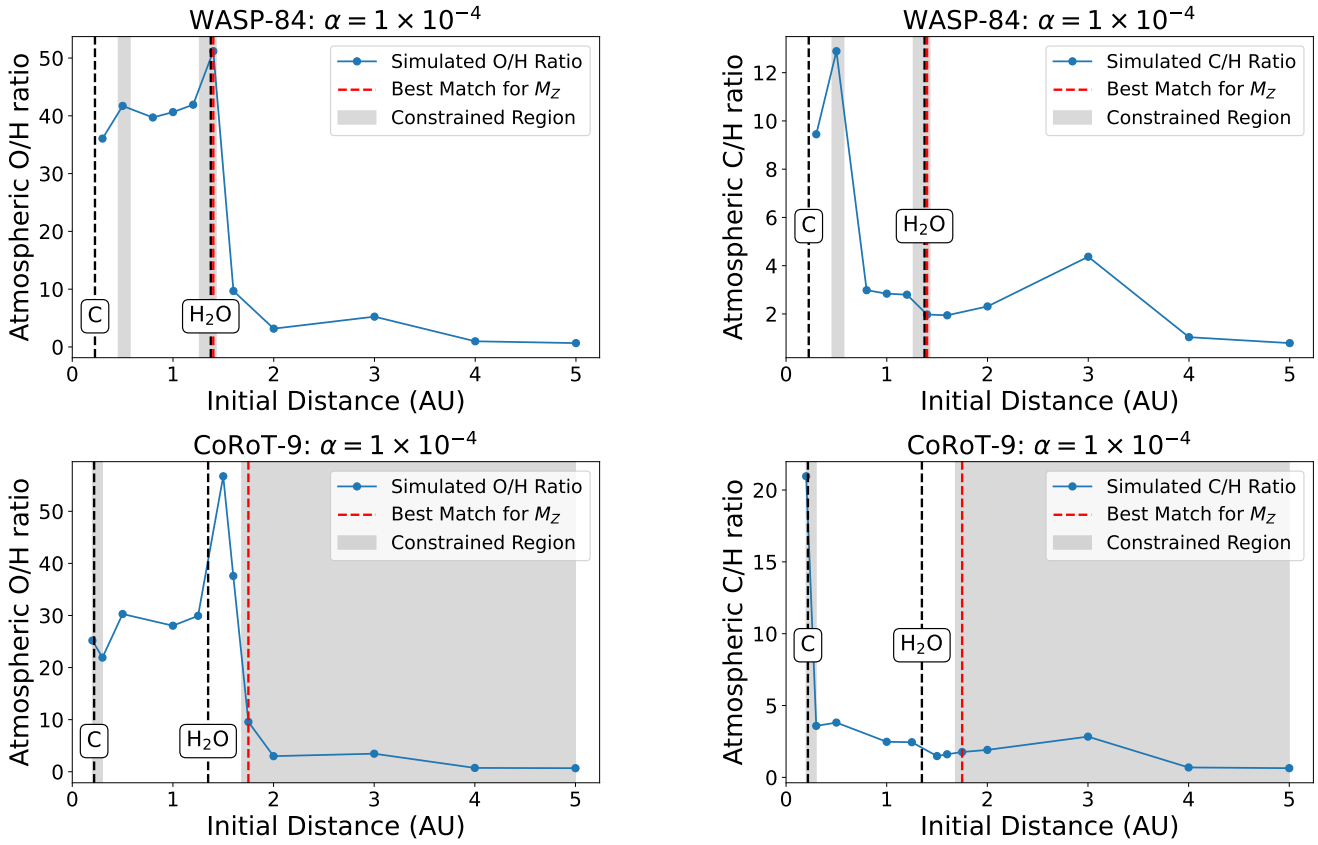

Fig. D.1. O/H and C/H (relative to the host star abundances) of the atmosphere of the planets simulated in the disc of WASP-84 (*top*) and CoRoT-9 (*bottom*) for varying initial positions of the planetary embryo in a disc of $\alpha = 1 \times 10^{-4}$. We show the formation location that resulted in the simulated heavy element mass of the planet matching most closely with the observation (dashed red line), the constrained regions where the planet could have initially formed (shaded grey regions), and the H_2O and C evaporation fronts (dashed black lines).